Journal of the Physical Society of Japan **92**, 114402 (2023)
https://doi.org/10.7566/JPSJ.92.114402

Design and Observation of Topological Band Gaps and Edge Modes of SOI Photonic Crystal Slabs in the Mid-Infrared Range

Afshan Begum[1,2], Yuanzhao Yao[3*], Takashi Kuroda[3], Yoshihiko Takeda[1,2], Naoki Ikeda[4], Yoshimasa Sugimoto[3], Takaaki Mano[3], and Kazuaki Sakoda[3†]

[1]*Center for Green Research on Energy and Environmental Materials, National Institute for Materials Science, Tsukuba, Ibaraki 305-0003, Japan*
[2]*Doctoral Program in Materials Science and Engineering, University of Tsukuba, Tsukuba, Ibaraki 305-8577, Japan*
[3]*Research Center for Functional Materials, National Institute for Materials Science, Tsukuba, Ibaraki 305-0044, Japan*
[4]*Research Network and Facility Service Division, National Institute for Materials Science, Tsukuba, Ibaraki 305-0047, Japan*

(Received November 4, 2022; accepted September 11, 2023; published online October 19, 2023)

We successfully materialized a complete common band gap of a 6.0% width relative to the mid-gap frequency for transverse-electric-like eigenmodes, which was shared by topologically trivial and non-trivial photonic crystals (PhCs) fabricated in the top Si layer of silicon-on-insulator wafers. We verified the presence of the complete common band gap, which is a prerequisite for the topologically protected edge mode, by angle-resolved reflection spectroscopy in the mid-infrared range. By applying polarization selection rules expected from the spatial symmetry of the electromagnetic eigenmodes, we confirmed the band inversion at the center of the first Brillouin zone (Γ point) in a purely experimental manner. We further detected the edge modes localized on the boundary between the trivial and non-trivial PhCs, which were linearly polarized in the vicinity of the Γ point due to the mixture of upper and lower branches with circular polarizations, and obtained their dispersion relation.

1. Introduction

Topological photonic crystals (PhCs), which imitate topological insulators,[1–5] have been attracting a great interest mainly because they can materialize helical one-way edge modes on the boundary between trivial and non-trivial PhCs.[6–15] They can be fabricated in PhC slabs,[7–19] that is, thin two-dimensional (2D) PhCs, which are often made of high-index semiconducting materials. Because the edge modes are topologically protected and free from back-scattering, they are expected to be new building blocks for high-performance optical circuits.

The PhC design for the helical edge modes was given by Wu and Hu.[6] They showed that the edge modes can be materialized on the boundary of 2D dielectric PhCs with the C_{6v} symmetry. They examined the photonic band structure of transverse magnetic (TM) eigenmodes and found that topologically non-trivial band gaps can be materialized between E_1 (dipole)- and E_2 (quadruple)-symmetric modes on the Γ point of the first Brillouin zone when the 2D PhCs have a slightly deformed honeycomb lattice while retaining the C_{6v} symmetry.

Barik et al. fabricated such 2D PhC slabs using air-bridged GaAs membranes,[7] for which an AlGaAs sacrificial layer under the membrane was removed by selective etching. Their PhC design was somewhat different from the original one by Wu and Hu, which was necessary for the 2D PhC slabs to open complete photonic band gaps for TE (transvers electric)-like modes.[8] They also confirmed the one-way propagation of the edge modes by observing two Zeeman components of the luminescence from InAs quantum dots integrated in the PhC slabs under static magnetic fields. Anderson and Subramania numerically examined the structural-parameter dependence of topological band gaps for membrane PhCs.[9] Kagami et al. investigated the coupling between Si wire waveguides and edge-mode waveguides.[10] For this purpose, they also numerically examined the structural-parameter dependence of the topological band gaps.

Unlike topological valley transport,[11,20,21] whose edge-mode dispersion curves are located below the light line so that the out-of-plane diffraction is absent and the quality (Q) factor is infinite, those edge modes in the vicinity of the Γ point possess finite Q factors due to the out-of-plane coupling to propagating waves in free space,[12–14] so they can be probed by using incident electromagnetic waves.

Gorlach et al.[13] and Parappurath et al.[14] reported such observations for silicon pillar PhCs on sapphire substrates and silicon membrane PhCs, respectively. The silicon pillar PhCs in Ref. 13 were sufficiently thick, so their sample design and dispersion relation were close to the purely 2D PhCs investigated in Ref. 6. On the other hand, a particular design like Refs. 7 and 8 was necessary for the silicon membrane PhCs mainly to prevent the band gap from closing on the M point in the first Brillouin zone.

Although the PhC membrane or air-bridged structure has advantages such as large photonic band gaps due to the large refractive-index contrast between air and dielectric materials consisting of the unit cell, their fabrication process is complicated and their mechanical strength is low. Recently Okada et al.[15] examined PhCs of the non-air-bridged structure fabricated in silicon-on-insulator (SOI) wafers and reported the variation of the dispersion curves of topologically trivial and non-trivial PhCs due to the changes in their structural parameters. Li et al.[16] examined polaritonic edge modes in transition metal dichalcogenide monolayers induced by the interaction with trivial and non-trivial PhCs having an arm-chair boundary between them, which was also non-membrane and fabricated in an SOI wafer, and observed their dispersion relation with circular polarizations.

In this paper, we report on the design and fabrication of trivial and non-trivial SOI PhCs that share a complete common band gap of a 6.0% width relative to the mid-gap frequency for TE-like modes. We proved the band inversion by observing the polarization dependence of the reflection spectra. We further proved the presence of the edge modes on a zig-zag boundary between the two PhCs by detecting

spectral dips in the mid-gap frequency range and confirmed that they were linearly polarized in the vicinity of the Γ point as predicted by numerical calculations.

This paper is organized as follows. In Sect. 2, we present the sample design based on our calculations of the dispersion relation by the finite element method (FEM). The sample fabrication by electron beam lithography is described in Sect. 3. The method to observe the bulk and edge modes is described in Sect. 4. The results of the measurements are presented in Sect. 5. A brief summary is given in Sect. 6.

2. Sample Design

Figure 1 is an illustration of our sample design together with the configuration of angle-resolved reflection measurements. We adopted triangular-lattice PhC structures to materialize complete photonic band gaps as in previous studies.[6–10,12–16] Their first Brillouin zone is illustrated in Fig. 1(a), while the top view of their unit cell is shown in Fig. 1(b). The PhC structure was fabricated in the top silicon layer of SOI wafers as shown in Fig. 1(c). The thickness of the top silicon layer and the SiO_2 layer was 0.4 and 3.0 μm, respectively according to available SOI wafers (SOITEC).

Although Wu and Hu showed the topological edge modes of deformed honeycomb PhCs with circular dielectric pillars for TM waves, we rather followed the recipe by Barik et al.[7,8] for the ease of sample fabrication and the formation of complete band gaps. That is, we designed and fabricated deformed honeycomb PhCs consisting of triangular air cylinders in the top Si layer, for which we may be able to materialize complete band gaps for TE-like modes by preventing the gaps from closing on the M point in the Brillouin zone. While Barik et al.[7,8] reported air-bridged GaAs PhC membranes, for which we need the under-etch of a sacrificial layer beneath the GaAs thin film, we tried to materialize topological edge modes with PhCs in SOI wafers without under-etching, which simplified the fabrication process much.

We start with a unit cell consisting of six identical triangular air cylinders in the top silicon layer of the SOI wafers with $a/R = 3$, where a is the lattice constant of the PhC and R is the distance between the center of the air cylinders and the center of the unit cell [see Fig. 1(b)]. At this point, we deform the unit cell to destroy the honeycomb symmetry ($a/R \neq 3$) by shifting the air cylinders, while keeping the C_{6v} symmetry. Thus, the degeneracy of E_1- and E_2-symmetric modes is lifted on the Γ point and we can control the Z_2 topology,[6] that is, we can materialize both trivial band gaps, for which the E_2-mode frequency is higher, and non-trivial band gaps, for which the E_1-mode frequency is higher, by adjusting R. In addition, we need to materialize complete band gaps throughout the whole Brillouin zone, which is a prerequisite for the edge modes. Fortunately, we found such structural parameters for the TE-like modes with a large band gap of a 5.7% width as we will describe in the following.

Before we show the dispersion relation of the specimens that we investigated, let us present the selection rules for reflection peaks. Due to the C_{6v} symmetry of our PhC structure, there are six mode symmetries, or irreducible representations, on the Γ point (see Table I).[22] Because the electric field is a genuine vector whereas the magnetic field is an axial vector, their symmetries are generally different. We refer to the symmetry of the magnetic field in Table I. Among the six mode symmetries, E_1 and E_2 modes are doubly degenerate, so there are two eigen functions for each of them. All modes except the E_1 (dipolar) mode are inactive to the incident light from normal direction [$\theta = 0°$, see Fig. 1(c)] due to their symmetry mismatch.[22] So, we can distinguish E_1 modes from E_2 modes by angle-resolved reflection measurements using this feature.[23–25] In addition, the PhC structure is symmetric about the x–z and y–z planes, so the eigen functions of modes with wave vectors in the x (Γ-to-K) and y (Γ-to-M) directions are characterized by the parity about these mirror planes, which leads to polarization selection rules listed in Table I.[25] Those modes which are active to p- (s-) polarized incident waves are denoted by p (s).

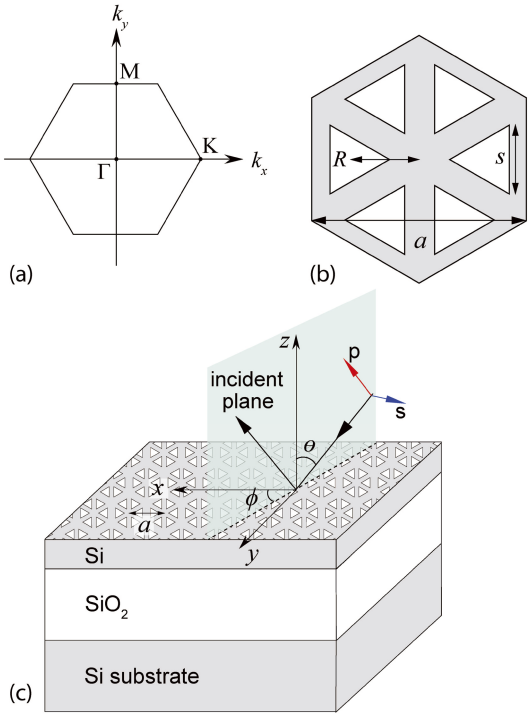

Fig. 1. (Color online) (a) The first Brillouin zone of the PhC specimens of the C_{6v} symmetry and (b) the top view of the unit cell, where a is the lattice constant, s is the side length of triangular air cylinders, and R is the distance between the center of the air cylinder and the center of the unit cell. (c) Configuration of the incident plane wave for the angle-resolved reflection measurement on the illustration of the specimen structure. θ and ϕ denote the tilt angle from the normal (z) direction and the azimuthal angle from the x axis, respectively. Two-dimensional photonic crystals were fabricated in the top silicon layer of SOI wafers.

Table I. Selection rules for reflection peaks. p and s denote that the modes are active to p and s polarizations, respectively. E_1 and E_2 modes are doubly degenerate, so there are two branches for each of them in both Γ-to-K and Γ-to-M directions. One branch is active to s polarization and the other is active to p polarization.

Mode on the Γ point	Γ ($\theta = 0°$)	Γ-to-K ($\phi = 0°$)	Γ-to-M ($\phi = 90°$)
A_1	inactive	s	s
A_2	inactive	p	p
B_1	inactive	s	p
B_2	inactive	p	s
E_1	active	s, p	s, p
E_2	inactive	s, p	s, p

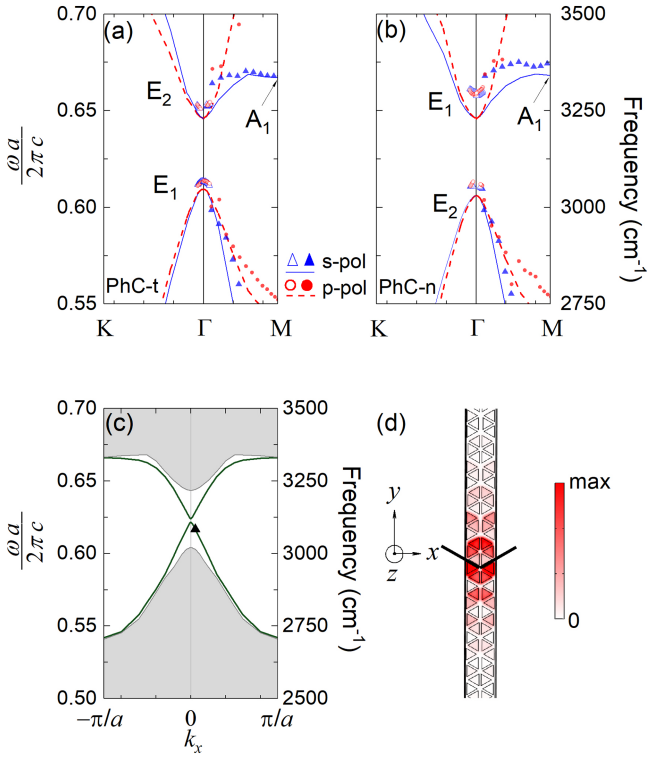

Fig. 2. (Color online) (a) Dispersion relation of TE-like modes for PhC-t and (b) PhC-n. Blue solid line and red broken line show calculated dispersion curves for s- and p-active modes, respectively. Blue open circle and red open triangle show data points measured by our home-made high-resolution setup for s and p polarizations, respectively, whereas blue solid circle and red solid triangle show those measured by Seagull for s and p polarizations, respectively. Designed structural parameters are as follows: $a = 2.0\,\mu$m, $s = 800\,$nm, $R = 620\,$nm for PhC-t and $R = 700\,$nm for PhC-n. The refractive indices of Si and SiO_2 were assumed to be 3.427[26] and 1.440,[27] respectively. (c) The calculated dispersion relation of edge modes (dark green line) and the spectral range of bulk modes (gray color). In each panel, the vertical axes are genuine (right) and normalized (left) frequencies, where ω is the angular frequency and c is the light velocity in free space, whereas the horizontal axis is the wave vector in the first Brillouin zone. k_x denoted the x component of the wave vector. (d) The time average of the square of the z component of the magnetic field plotted for an edge mode denoted by a solid triangle in panel (c).

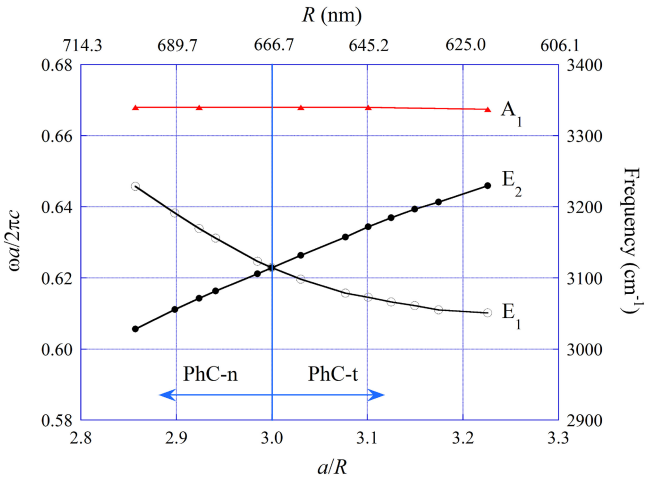

Fig. 3. (Color online) The R dependence of the eigen frequencies. a and s were fixed at 2.0 μm and 800 nm, respectively. The E_1 and E_2 modes on the Γ point are plotted with open and solid black circles, respectively. The A_1 mode on the M point is plotted with solid red triangles. For a/R smaller (larger) than three, the gap is non-trivial (trivial).

First, we examined two specimen designs denoted by PhC-t and PhC-n, for which we found a common band gap from 3049 to 3229 cm^{-1} by the following numerical calculation. This band gap amounts to 5.7% of the mid gap frequency. Figures 2(a) and 2(b) show their dispersion relation for TE-like modes calculated (solid and broken lines) by FEM using the commercial software COMSOL Multiphysics and experimental observations (circles and triangles), the latter of which will be described later. The dispersion curves with red broken lines and blue solid lines represent p- and s-active modes, respectively. The structural parameters of these calculations are given in the figure caption. For the numerical calculations, we imposed the Bloch boundary condition on the unit cell surface in the lateral (x and y) directions and the PML (perfectly matched layer) absorbing boundary condition at its two vertical ends, $z = 3.7$ and $-6.7\,\mu$m, where the origin of the z coordinate is set at the center of the top Si layer. The eigen frequency of the A_1-symmetric mode on the M point is larger than the E_1 and E_2 mode frequencies on the Γ point, so the band gaps are defined by the latter two modes. As we can see, trivial and non-trivial complete band gaps are materialized for PhC-t and PhC-n, respectively, which overlap each other to give a common band gap of a 5.7% width relative to the mid-gap frequency. Consequently, we can materialize topologically protected edge modes on the boundary between the two PhCs due to the bulk-edge correspondence.[6] Their dispersion curves are presented by dark green lines in Fig. 2(c), whereas the gray color denotes the frequency ranges of bulk modes. In these figures, the vertical axes are genuine (right) and normalized (left) frequencies, where ω is the angular frequency and c is the light velocity in free space. The horizontal axis is the wave vector in the first Brillouin zone. In Fig. 2(c), k_x denotes the x component of the wave vector.

The 5.7% width of the complete common band gap is larger than the cases of PhC membranes, that is, 4.1% in Ref. 8 and 4.7% in Ref. 14 in spite of the smaller refractive-index contrast of our specimens. This is because the band gap is not only dependent on the refractive-index contrast but also dependent on the degree of symmetry breaking described by R, since the band gap vanishes for the symmetric case of the honeycomb lattice.

Figure 3 shows the R dependence of the eigen frequencies on the Γ and M points. For the Γ point, the E_1 and E_2 modes are plotted, which determine the trivial and non-trivial band gaps. For the M point, the A_1 mode close to the upper band-gap-edge (see Fig. 2) is plotted, which may affect the band gap. The A_1 mode frequency is larger than the E_1 and E_2 mode frequencies for all R values that we examined, so the band gap is defined by the E_1 and E_2 modes. By the combination of $R = 700\,$nm (PhC-n) and $R = 620\,$nm (PhC-t), we can achieve a 5.7% common band gap as we mentioned. When we increase or decrease R further, we may obtain larger band gaps. In that case, however, the distance between adjacent triangular air cylinders become too small to achieve accurate sample fabrication.

The edge-mode dispersion shown in Fig. 2(c) was calculated by assuming 11 unit cells of PhC-t on the upper side ($y > 0$) and PhC-n on the lower side ($y < 0$) of the

boundary along the x axis. We assumed the Bloch boundary condition in the x direction and PML absorbing boundary condition in the y and z directions. Note that there is a small gap of 12 cm^{-1} between two edge-mode dispersion curves on the Γ point, which originates from the mode mixing due to the lack of inversion symmetry around the boundary between the two PhCs.[6)] To examine the localized nature of the edge-mode eigen function, the time average of the square of the z component of the magnetic field at the center of the top Si layer ($z = 0$) is drawn in Fig. 2(d) for the edge mode denoted by a triangle in Fig. 2(c), where a thick black wedge emphasizes the location of the boundary between the two PhCs. This figure clearly shows the edge-mode localization around the boundary. By curve fitting, the localization length was estimated to be 3.6 times the lattice constant.

Figure 4 is the far-field polarization of the edge modes calculated at $z = 16.4\,\mu m$. The PML was located at sufficiently large z for this particular calculation. Each panel shows the endpoint of the electric field during one period of the electromagnetic-field oscillation. Because the vicinity of the Γ point is important in this study, the polarization was examined for $0 \le k_x \le 0.008 \times 2\pi/a$. As panel (a) and (b) show, the far filed is linearly polarized at $k_x = 0$ for both lower and upper branches due to the 1 : 1 mixture of the right- and left-circular polarizations caused by the anti-crossing of the two edge-mode dispersion curves, which is a direct consequence of the spin mixing discussed in Ref. 6. The far field approaches to its original circular polarization with increasing $|k_x|$.

3. Sample Fabrication

According to the sample design in the previous section, we fabricated the specimens by standard electron beam lithography (Elionix, ELS-125) of SOI wafers (SOITEC) with high-contrast e-beam resist (Allresist, AR-P6200) and exposure parameters of accelerating voltage 125 kV, current of 1 nA, field size 250 μm, 50,000 dot numbers and a shot time of 0.06 μsec/dot of 240 $\mu C/cm^2$ dose. The pattern was developed at room temperature in xylene for 90 s, followed by IPA (isopropyl alcohol) wash for 30 s with slow puddling. Then we performed through-etching of 400 nm depth using DRIE (deep reactive ion etching) Bosch process with 27 cycles, having an etch rate of 15.14 nm/cycle. Figure 5(a) is a cross-sectional SEM image of one of the samples at this stage, showing the acquired smooth vertically etched walls. The residue resist was removed by twenty-minute dip in 80 °C organic solvent NMP (N-methyl-2-pyrrolidone), followed by acetone wash, IPA wash and plasma ashing.

We fabricated the trivial (PhC-t) and non-trivial (PhC-n) bulk samples on one SOI wafer. Their size was 3 mm by 3 mm. The top view of the PhCs is presented in Figs. 5(b) and 5(c), revealing sharp vertices of the triangular holes and consistent side length s that were achieved in the fabrication. These sharp vertices are essential to open the band gap for TE-like modes.[7,8,15)]

We fabricated another sample of 4 mm by 4 mm that consisted of repetitive arrays of zig-zag boundaries between the trivial and non-trivial PhCs, which we call combination specimen hereafter. Each zig-zag boundary is made up of 25 unit cells of trivial and non-trivial PhCs on either side. Figure 5(d) shows an SEM image of one of the zig-zag

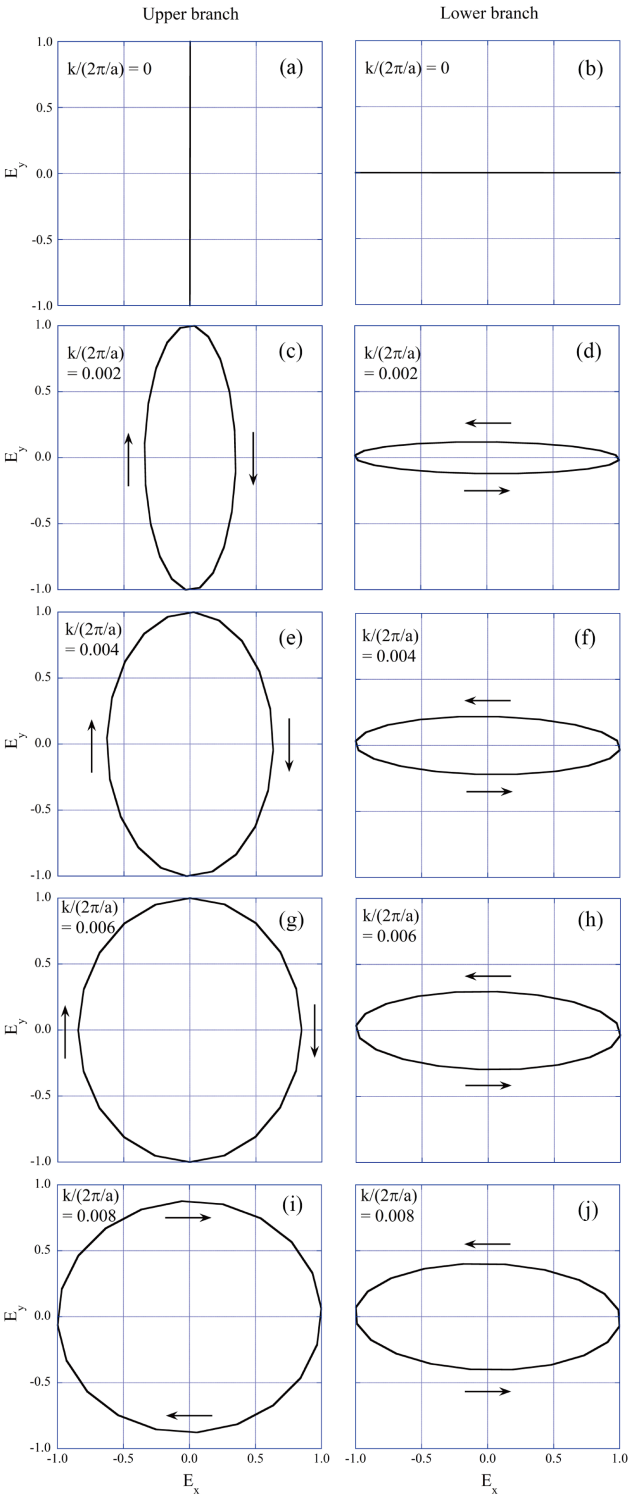

Fig. 4. (Color online) Far-field polarization of the edge modes of the lower (right column) and upper (left column) branches. The far field was evaluated at $z = 16.4\,\mu m$ on the border between the two PhCs. The figures show the endpoint of the electric field in the horizontal plane, which is normalized by its maximum value, during one period of the electromagnetic-field oscillation. Arrows show the direction of the polarization rotation.

boundaries, where the difference in R for the two PhCs is clearly seen.

4. Measurements

Reflection spectra in the mid-infrared range was measured with an FT-IR spectrometer (JASCO, FT/IR-6800) with a 2.0 cm^{-1} spectral resolution. For angle-resolved reflection

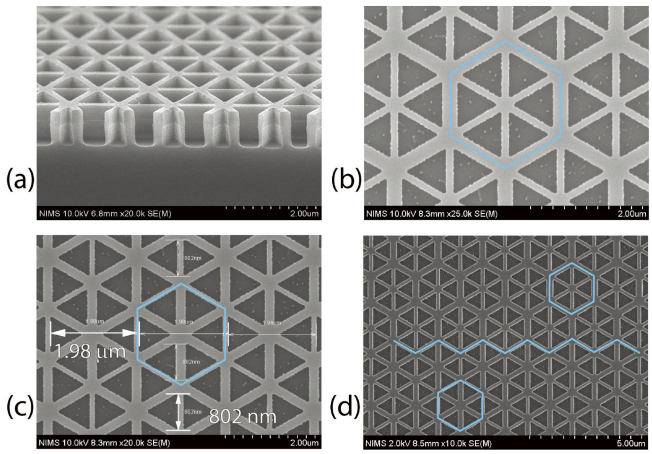

Fig. 5. (Color online) SEM images of fabricated specimens. (a) Cross-sectional view after etching. Top view of (b) PhC-t and (c) PhC-n. (d) Top view of the combination specimen. The zig-zag boundary between PhC-t and PhC-n and their unit cells are highlighted by blue lines.

measurements around the Γ point of the first Brillouin zone, we used our home-made optical setup to materialize a 0.3° angle resolution,[28,29] which was fitted inside the sample chamber of the FT-IR, while we used Seagull (Harrick Scientific) for measurements with 5 to 70° incident angles. We also used an IR microscope (JASCO, IRT-5200) to measure the normal-incidence reflection with a reduced angle resolution. For polarization-dependent reflection measurements, we used a nanoparticle-film polarizer.

5. Results and Discussions

5.1 Bulk modes

Figure 6(a) shows the reflection spectra of PhC-t measured by our home-made angle-resolved FT-IR setup. The incident angle was tuned from $\theta = -3.79$ to $+4.08°$. They were measured in the Γ-to-K ($\phi = 0°$) and Γ-to-M ($\phi = 90°$) directions for both s and p polarizations. Each panel in Fig. 6(a) consists of 28 reflection spectra measured with a 0.292° step incident angle (θ). The upper and lower limits of the lowest reflection spectrum are 1 and 0, respectively. Other spectra are drawn in the same scale and shifted by 0.1 in the vertical direction.

In each spectrum, one or two sharp peaks of the Fano-type resonance are superimposed on the large background undulations, the latter of which are caused by the interference of the Si and SiO_2 multilayers in the SOI wafer. The sharp Fano-type peaks originate from the resonant reflection by the PhC eigenmodes, so their dispersion relation can be obtained by plotting the resonance frequency against the lateral component of the incident wave vector. Each resonance frequency was obtained by curve fitting to the observed spectrum with a combination of an asymmetric Lorentzian (Fano) function for the PhC eigenmode and a polynomial function for the background undulation.

The data points thus obtained are plotted (open circles and triangles) around the Γ point in Fig. 2(a), whose frequencies are close to the calculated dispersion curves. The maximum discrepancy was as small as 0.32%, which is evidence for an

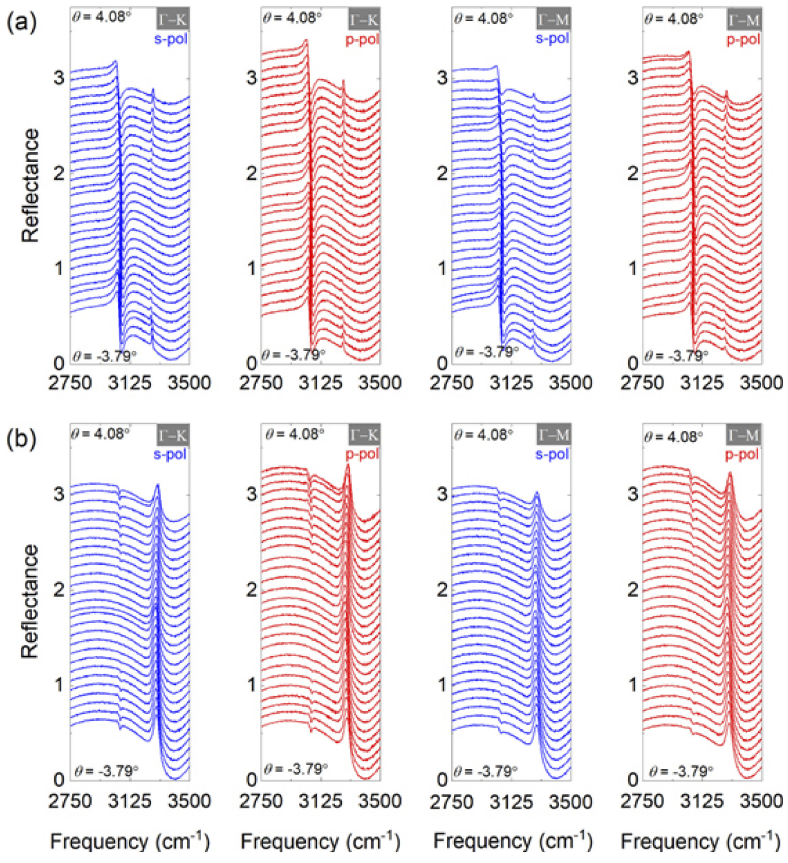

Fig. 6. (Color online) Angle-resolved reflection spectra of (a) PhC-t and (b) PhC-n measured in the Γ-to-K ($\phi = 0°$) and Γ-to-M directions ($\phi = 90°$) for both s and p polarizations by our home-made high-resolution setup. Each panel consists of 28 spectra measured for different incident angles (θ) in 0.292° steps. The upper and lower limits of the lowest reflection spectrum in each panel are 1 and 0, respectively. Other spectra are drawn in the same scale and shifted by 0.1 in the vertical direction.

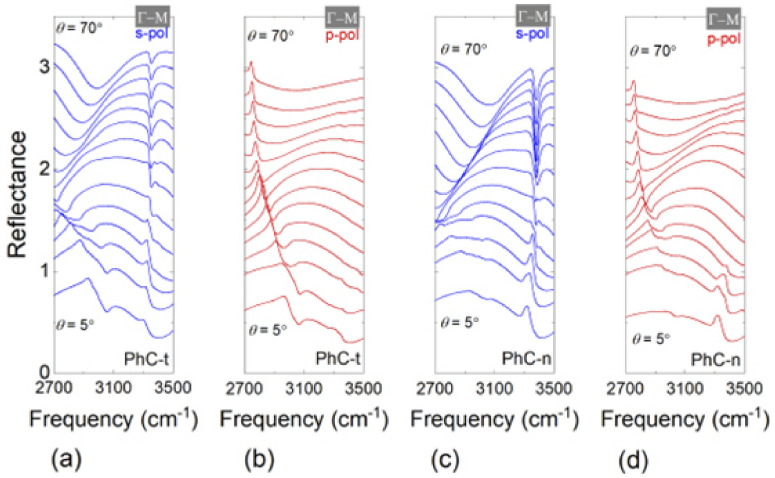

Fig. 7. (Color online) Angle-resolved reflection spectra measured in the Γ-to-M direction ($\phi = 90°$) for (a), (b) PhC-t and (c), (d) PhC-n for both s and p polarizations by the commercial variable-angle reflection accessory, Seagull. Each panel consists of 14 spectra measured for different incident angles (θ) in 5° steps. The upper and lower limits of the lowest reflection spectrum in each panel are 1 and 0, respectively. Other spectra are drawn in the same scale and shifted by 0.15 in the vertical direction.

accurate sample fabrication. Another important feature of the observed reflection spectra is that the Fano-type resonance peaks disappear at the Γ point ($\theta = 0°$) for the higher-frequency component around 3250 cm^{-1}, while they do not disappear for the lower-frequency component around 3050 cm^{-1}. By keeping it in mind that each component consists of both s- and p-active modes and consulting the selection rules in Table I, we can conclude that the high and low frequency components originate from E_2 and E_1 modes, respectively. So, this band gap is a trivial one.

To examine whether this band gap is a complete gap, we measured reflection spectra for larger incidence angles ($\theta =$ 5–70°) with Seagull in the Γ-to-M direction, since the band gap does not decrease but rather increases in the Γ-to-K direction, so a possible gap closing takes place only in the Γ-to-M direction. The reflection spectra are presented in Figs. 7(a) and 7(b). The spectral width of the Fano-type resonance peaks is generally larger than that of Fig. 6 mainly because the angle resolution of our home-made setup is better than Seagull. For the reflection spectra in Figs. 7(a) and 7(b), the resonance frequency was estimated by the average of the local minimum and maximum frequencies of each Fano-type resonance peak. Their data points are also plotted (solid circle and triangle) in Fig. 2(a). We can clearly see that the photonic band gap found around the Γ point is kept open all the way to the M point. Thus, we confirmed the complete band gap of the TE-like modes for PhC-t.

Next, we present the same analysis for PhC-n. Figure 6(b) shows the angle-resolved reflection spectra around the Γ point. It is clearly observed that the resonance frequencies of the active (E_1) and inactive (E_2) modes are reversed in this case, which is clear evidence for the topologically non-trivial band gap. The data points are plotted (open circles and triangles) in Fig. 2(b) together with those obtained by Seagull (solid circles and triangles), whose spectra are shown in Figs. 7(c) and 7(d). The agreement between the observed and calculated frequencies is again good, although the discrepancy is somewhat larger than PhC-t, which is 1.5% around the Γ point.

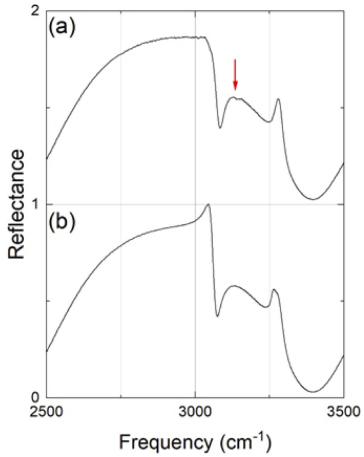

Fig. 8. (Color online) (a) Normal-incidence reflection spectrum of the edge-mode specimen measured by micro FT-IR, where the red arrow points to a small dip in the common gap frequency range, which may indicate an edge mode on the Γ point. (b) The arithmetic average of normal incidence reflection spectra of PhC-t and PhC-n. Two peaks around 3050 and 3300 cm^{-1} show the lower and upper edges of the common gap.

By comparing Figs. 2(a) and 2(b), we can conclude that the trivial (PhC-t) and non-trivial (PhC-n) specimens share a common band gap from 3068 to 3257 cm^{-1}, which amounts to 6.0% of the mid gap frequency. This value is very close to the theoretical design, 5.7%, in Sect. 2. By the bulk-edge correspondence,[6] we can expect the presence of the topologically protected edge modes localized on the boundary between the two PhCs as shown in Figs. 2(c) and 2(d).

5.2 *Edge modes*

First, we tried micro FT-IR measurements from the normal (z) direction with an IR microscope. The angle resolution was estimated at 5°. Figure 8(a) shows the measured spectrum together with the average of the reflection spectra of bulk PhC-t and PhC-n as a reference, Fig. 8(b). By comparing these two spectra, we find a small new feature in the common band gap range, which is denoted by a red arrow. This small dip is caused by the edge mode on the Γ point, although the

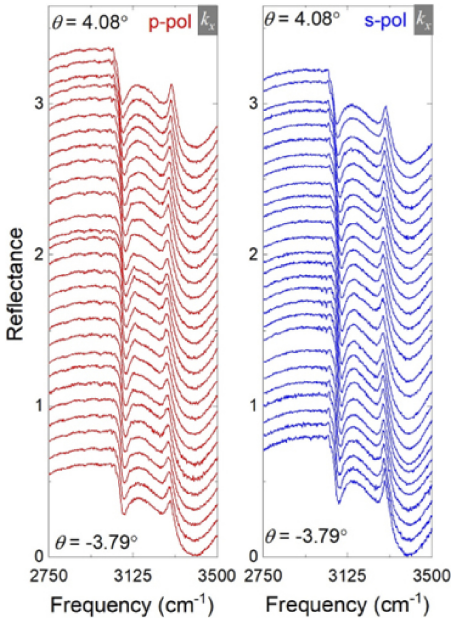

Fig. 9. (Color online) Angle-resolved reflection spectra for the combination specimen. Incident angles were varied from $\theta = -3.79$ to 4.08° for both p polarization (left panel, red color) and s (right panel, blue color) polarizations. The incident beam was tilted in the x direction along the boundary between PhC-t and PhC-n. 28 spectra were measured for each polarization in 0.292° steps. The upper and lower limits of the lowest reflection spectrum are 1 and 0, respectively. Other spectra are drawn in the same scale and shifted by 0.1 in the vertical direction.

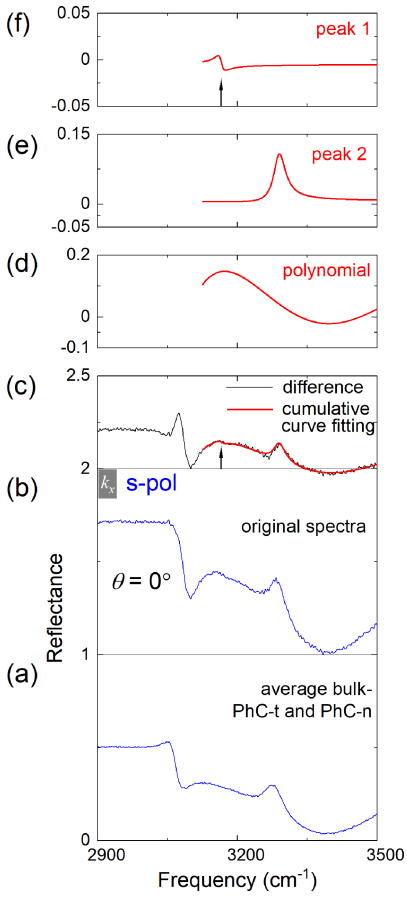

Fig. 10. (Color online) Illustration of the curve fitting procedure. (a) The averaged reflection spectrum of PhC-t and PhC-n. (b) The reflection spectrum of the combination specimen. (c) Their difference (black line) and the results of the curve fitting (red line). (d)–(f) Three components used for the curve fitting. The black arrow denotes the resonance frequency of the mid-gap mode. The case of $\theta = 0°$ and s polarization is illustrated as an example.

two modes of the upper and lower branches are not resolved due to a lower angle resolution of 5°.

Next, Fig. 9 shows the angle-resolved reflection spectra of the combination specimen measured with our high-resolution setup. In addition to two distinct sharp resonance peaks around 3070 and 3300 cm^{-1}, which originate from the E_1 modes of PhC-t and PhC-n, respectively, an additional dip is observed in the band gap frequency range in each spectrum for both p (left panel, red lines) and s (right panel, blue lines) polarizations, although the dips are very shallow for s polarization. This small dip is caused by the topological edge mode as we will show in the following. On the other hand, a few dips found at frequencies less than 3070 cm^{-1} originate from the discretized bulk modes due to the periodic arrangements of PhC-t and PhC-n of 25 unit cells in the y direction.

To reproduce the dispersion relation of the edge modes, we did a curve fitting as described in Fig. 10. First, we calculated the difference between the reflection spectrum of the combination specimen and the averaged spectrum of PhC-t and PhC-n to eliminate the E_1-mode peaks and enhance the mid-gap dips. Although the E_1-mode peaks could not be completely eliminated because the E_1 modes in the combination specimen is not exactly the same as those in PhC-t or PhC-n due to the periodic arrangement of their 25 unit cells, the mid-gap dip was relatively emphasized. Then the background undulation was approximated with a third-order polynomial, while the mid-gap dip and the E_1-mode peak were approximated with asymmetric Lorentzian (Fano) functions.

We now present the dispersion of the edge modes obtained by mapping the resonance frequency against the lateral component of the incident wave vector in Fig. 11. The red and blue closed triangles denote the p- and s-active mid-gap modes, whereas the green lines are the dispersion curves calculated by FEM. The number of data points is smaller for the s polarization, since we only plotted such resonance frequencies that were clearly identified by the curve fitting. As we described with Fig. 4, the upper and lower branches of the edge modes are expected to be active to s and p polarizations, respectively in the vicinity of $k_x = 0$. So, our observation is consistent with this theoretical result. The observed frequencies are close to the numerical results. Their discrepancy was smaller than 1.5%, which is evidence for our accurate calculation and sample fabrication.

On the other hand, for increasing $|k_x|$, both upper and lower branches return to their original circular polarization as shown in Fig. 4, so they become active to both s and p polarizations. This behavior is observed in Fig. 9. For example, we can find spectral changes around 3125 cm^{-1} in the lowest six reflectance curves for the s polarization, which originate from spectral dips of the lower edge-mode branch. However, these dips are close to the large E_1-mode peak around 3070 cm^{-1}, so there was a relatively big ambiguity in the identification of their frequencies even when we did the curve fitting. Then in Fig. 11, we plotted only one data point obtained from an s-polarization spectrum (open blue triangle), which we think originates from the lower edge-

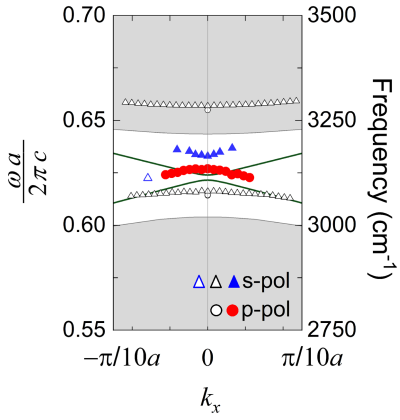

Fig. 11. (Color online) The dispersion relation of the edge modes. The vertical axes are genuine (right) and normalized (left) frequencies, while the horizontal axis is the wave vector in the x direction. The green lines are the calculated dispersion curves, whereas the red and blue closed triangles denote the resonance frequency of the mid-gap mode obtained by the curve fitting to the angle-resolved reflection spectra for p- and s-active modes, respectively. Note that the upper and lower edge-mode branches are circularly polarized for large $|k_x|$, so they are active to both s and p polarizations (see Fig. 4). By this reason, the lower branch was also detected by the s polarization. One such data point is plotted with an open blue triangle. The open black triangles and circles denote the resonance frequency of the s- and p-active gap-edge modes, respectively, whereas the gray regions denotes the calculated frequency ranges of the bulk modes.

mode branch. Its frequency looks consistent with the edge-mode dispersion curve obtained by the p-polarized reflectance (solid red circle).

In Fig. 11, the resonance frequencies of the gap-edge modes are also plotted with open black triangles and circles. They correlate well with the boundaries of the frequency ranges of the bulk modes calculated by FEM, which are shown with a gray color. Because the gap-edge modes in the combination specimen is not exactly the same as the E_1 modes of the bulk specimens, this correlation is originally approximate.

6. Conclusion

We found a specimen design to achieve a complete common band gap of topologically trivial and non-trivial PhCs (PhC-t and PhC-n) with a 5.7% relative width for the TE-like modes by FEM calculations, which can be fabricated in an SOI wafer without under-etching of the top silicon layer. This design materializes helical one-way edge modes localized on the boundary between the two PhCs in a usual platform of the silicon photonics and greatly simplifies the fabrication process. We also numerically analyzed the polarization of the far field of the edge modes and found that their upper and lower branches are linearly polarized in the vicinity of the Γ point due to the 1 : 1 mixture of their original left- and right-circular polarizations.

We fabricated these PhC specimens by electron beam lithography and confirmed the complete common band gap of a 6.0% width by angle-resolved reflection measurements in the mid-infrared range, which was close to the theoretical calculation. By using the polarization selection rules, we detected the band inversion in a purely experimental manner.

We also fabricated a combination specimen consisting of alternating PhC-t and PhC-n structures. We succeeded in observing the mid-gap resonance dips in the angle-resolved reflection spectra and obtained the edge-mode dispersion relation. The upper and lower branches were active to s and p polarizations around $k_x = 0$ as predicted by the numerical calculation.

Acknowledgments This work was supported by the Innovative Science and Technology Initiative for Security, Grant Number JPJ004596, ATLA, Japan. A.B. acknowledges support from the NIMS Graduate Research Assistantship program.

Author contribution A. Begum and Y. Yao contributed equally.

*Present address: *Department of Applied Physics, University of Tsukuba, Tsukuba 305-8573, Japan*
†sakoda.kazuaki@nims.go.jp

1) C. L. Kane and E. J. Mele, Phys. Rev. Lett. **95**, 226801 (2005).
2) B. A. Bernevig, T. L. Hughes, and S.-C. Zhang, Science **314**, 1757 (2006).
3) D. Hsieh, D. Qian, L. Wray, Y. Xia, Y. S. Hor, R. J. Cava, and M. Z. Hasan, Nature **452**, 970 (2008).
4) M. Z. Hasan and C. L. Kane, Rev. Mod. Phys. **82**, 3045 (2010).
5) X.-L. Qi and S.-C. Zhang, Rev. Mod. Phys. **83**, 1057 (2011).
6) L. H. Wu and X. Hu, Phys. Rev. Lett. **114**, 223901 (2015).
7) S. Barik, A. Karasahin, C. Flower, T. Cai, H. Miyake, W. D. Gottardi, M. Hafezi, and E. Waks, Science **359**, 666 (2018).
8) S. Barik, H. Miyake, W. DeGottardi, E. Waks, and M. Hafezi, New J. Phys. **18**, 113013 (2016).
9) P. D. Anderson and G. Subramania, Opt. Express **25**, 23293 (2017).
10) H. Kagami, T. Amemiya, S. Okada, N. Nishiyama, and X. Hu, Opt. Express **28**, 33619 (2020).
11) X.-T. He, E.-T. Liang, J.-J. Yuan, H.-Y. Qiu, X.-D. Chen, F.-L. Zhao, and J.-W. Dong, Nat. Commun. **10**, 872 (2019).
12) E. Sauer, J. P. Vasco, and S. Hughes, Phys. Rev. Res. **2**, 043109 (2020).
13) M. A. Gorlach, X. Ni, D. A. Smirnova, D. Korobkin, D. Zhirihin, A. P. Slobozhanyuk, P. A. Belov, A. Alù, and A. B. Khanikaev, Nat. Commun. **9**, 909 (2018).
14) N. Parappurath, F. Alpeggianil, K. Kuipers, and E. Verhagen, Sci. Adv. **6**, eaaw4137 (2020).
15) S. Okada, T. Amemiya, H. Kagami, Y. Wang, N. Nishiyama, and X. Hu, J. Opt. Soc. Am. B **39**, 2464 (2022).
16) M. Li, I. Sinev, F. Benimetskiy, T. Ivanova, E. Khestanova, S. Kiriushechkina, A. Vakulenko, S. Guddala, M. Skolnick, V. M. Menon, D. Krizhanovskii, A. Alù, A. Samusev, and A. B. Khanikaev, Nat. Commun. **12**, 4425 (2021).
17) P. L. Gourley, J. R. Wendt, G. A. Vawter, T. M. Brennan, and B. E. Hammons, Appl. Phys. Lett. **64**, 687 (1994).
18) O. Painter, R. K. Lee, A. Scherer, A. Yariv, J. D. O'Brien, P. D. Dapkus, and I. Kim, Science **284**, 1819 (1999).
19) T. Kuroda, N. Ikeda, T. Mano, Y. Sugimoto, T. Ochiai, K. Kuroda, S. Ohkouchi, N. Koguchi, K. Sakoda, and K. Asakawa, Appl. Phys. Lett. **93**, 111103 (2008).
20) A. M. Dubrovkin, U. Chattopadhyay, B. Qiang, O. Buchnev, Q. J. Wang, Y. Chong, and N. I. Zheludev, Appl. Phys. Lett. **116**, 191105 (2020).
21) S. Arora, T. Bauer, R. Barczyk, E. Verhagen, and L. Kuipers, Light: Sci. Appl. **10**, 9 (2021).
22) K. Sakoda, *Optical Properties of Photonic Crystals* (Springer, Berlin, 2004) 2nd ed.
23) S. Chalimah, Y. Yao, N. Ikeda, Y. Sugimoto, T. Mano, T. Kuroda, and K. Sakoda, Opt. Express **29**, 19486 (2021).
24) A. Begum, Y. Yao, T. Kuroda, E. Watanabe, N. Ikeda, Y. Sugimoto, Y. Takeda, and K. Sakoda, J. Phys. Soc. Jpn. **91**, 084401 (2022).
25) Y. Yao, T. Kuroda, N. Ikeda, T. Mano, H. Koyama, Y. Sugimoto, and K. Sakoda, Opt. Express **28**, 21601 (2020).
26) D. Chandler-Horowitz and P. M. Amirtharaj, J. Appl. Phys. **97**, 123526 (2005).
27) I. H. Malitson, J. Opt. Soc. Am. **55**, 1205 (1965).
28) T. Kuroda, S. Chalimah, Y. Yao, N. Ikeda, Y. Sugimoto, and K. Sakoda, Appl. Spectrosc. **75**, 259 (2021).
29) Y. Yao, N. Ikeda, T. Kuroda, T. Mano, H. Koyama, Y. Sugimoto, and K. Sakoda, Opt. Express **28**, 4194 (2020).